Dalton Transactions

ROYAL SOCIETY OF CHEMISTRY

PAPER

View Article Online
View Journal | View Issue

Cite this: *Dalton Trans.*, 2025, **54**, 784

$Yb_5Rh_6Sn_{18}$: a valence fluctuating system with ultra-low thermal conductivity†

Oleksandr Bolielyi,[a] Volodymyr Levytskyi,[a] Jörg Wagler,[b] Kristina O. Kvashnina,[c,d] Bohdan Kundys,[e] Andreas Leithe-Jasper[f] and Roman Gumeniuk*[a]

Received 30th September 2024,
Accepted 8th November 2024

DOI: 10.1039/d4dt02759k

rsc.li/dalton

$Yb_5Rh_6Sn_{18}$ crystallizes with a unique structural arrangement [space group $P4_2/nmc$, a = 9.6997(4) Å, c = 13.7710(7) Å], which is related with primitive cubic $Yb_3Rh_4Sn_{13}$ and body-centered tetragonal ($Sn_{1-x}Tb_x$)$Tb_4Rh_6Sn_{18}$ types. X-ray absorption spectroscopy showed that Yb atoms exhibit temperature-dependent valence fluctuations (VF) (*i.e.*, intermediate valence state). Its complex mechanism is corroborated by the fact that the well-pronounced maximum in magnetic susceptibility can only be fairly described by the Bickers–Cox–Wilkins model developed for a J = 3/2 multiplet, atypical for Yb ions. Both Hall and Seebeck coefficients revealed a switch of the sign, indicating the change of charge carrier type from electrons to holes between 120 and 220 K. Both these effects together with electrical resistivity and theoretical DFT calculations confirm $Yb_5Rh_6Sn_{18}$ to be a metal, which disobeys the free electron gas theory. 'Rattling' motion of Sn1 atoms within the enlarged 16-vertices distorted Frank–Kasper polyhedra, concluded from the specific heat measurements, is argued to be the main reason for the appearance of a phonon resonance behavior, resulting in an ultra-low thermal conductivity in the studied stannide.

1 Introduction

Intermetallics containing 4f rare-earth elements are known to tend towards magnetically ordered states defined by the Ruderman–Kittel–Kasuya–Yosida (RKKY) interaction. Its strength depends on the number of 4f electrons (n_f) as well as their position relative to the Fermi level (E_F), which determines the degree of localization. The competing scenario is the formation of a non-magnetic Fermi liquid ground state commonly referred to as the Kondo effect. Obviously, the decisive role in such a competition is played by the level of hybridization of 4f electrons with the conduction band states. Frequently it results in some exciting features like heavy fermions, quantum criticality, non-Fermi liquid state, spin and valence fluctuations [*i.e.*, intermediate valence state (IVS)], *etc.*[1–4]

The latter effect is observed in intermetallics containing rare-earth ions, revealing both non-magnetic (*e.g.*, Ce^{4+}, Eu^{3+}, and Yb^{2+}) and magnetic (*e.g.*, Ce^{3+}, Eu^{2+}, and Yb^{3+}) states. In some cases, such an ion can switch between configurations, resulting in a non-integer valence that is usually temperature dependent.[5,6] All these indicate the change of the ground state of the ion and its degeneracy (N), which is reflected in well-pronounced maxima in magnetic susceptibility and specific heat capacity. To simulate them, some theories, based on the Anderson and Kondo impurity models accounting for the hybridization strength,[7,8] are normally applied. For instance, using a unified approach for the former one, which assumes a simplified concept of large angular momentum degeneracy, Bickers, Cox and Wilkins[9] successfully simulated static properties. The Bethe *ansatz*, allowing determination of exact wave functions for quantum many-body models,[10] is a powerful tool in the solution of both the abovementioned models. So, generalization of the Kondo impurity approach for an N-fold degenerate state and application of the Bethe *ansatz* allowed the solution of the SU (N) Coqblin–Schrieffer model, which described well the properties of such impurities in a metal as Ce^{3+} (N = 6) and Yb^{3+} (N = 8).[11,12] Furthermore, it was extended

[a]*Institut für Experimentelle Physik, TU Bergakademie Freiberg, Leipziger Straße 23, 09596 Freiberg, Germany. E-mail: roman.gumeniuk@physik.tu-freiberg.de*
[b]*Institut für Anorganische Chemie, TU Bergakademie Freiberg, Leipziger Straße 29, 09599 Freiberg, Germany*
[c]*The Rossendorf Beamline at ESRF, CS 40220, 38043 Grenoble Cedex 9, France*
[d]*Helmholtz-Zentrum Dresden-Rossendorf (HZDR), Institute of Resource Ecology, P.O. Box 510119, 01314 Dresden, Germany*
[e]*Université de Strasbourg, CNRS, Institut de Physique et Chimie des Matériaux de Strasbourg, UMR 7504, Strasbourg F-67000, France*
[f]*Max-Planck-Institut für Chemische Physik fester Stoffe, Nöthnitzer Straße 40, 01187 Dresden, Germany*

†Electronic supplementary information (ESI) available. CCDC 2383845. For ESI and crystallographic data in CIF or other electronic format see DOI: https://doi.org/10.1039/d4dt02759k

to a complete range of temperatures and fields.[13] However, despite all these successes, none of the discussed models accounts for crystal electric field (CEF) multiplets splitting at non-zero temperatures. Being in the order of a few eV,[14] the splitting energy influences strongly the magnetic susceptibility and specific heat capacity. There is an attempt of theoretical simulation of such an effect; however, it is done only for the ions with a degeneracy of $N = 4$.[15] Among the known examples, where the theories fail in the description of temperature dependence of magnetic susceptibilities, we would like to mention YbCuAl,[16–18] YbB_{12},[19] $YbNi_2Ge_2$ and $YbPd_2Si_2$.[20]

In the past decades, numerous compounds have been found to be isostructural to the primitive cubic $Yb_3Rh_4Sn_{13}$ structure type discovered by Remeika and co-workers.[21] Furthermore, several intermetallics are shown to be its distorted variants with the same composition (such a structural relationship is normally explained within the group–subgroup scheme[22–27]) or with a close composition.[28–30] The majority of the latter compounds crystallize with the body-centered tetragonal $(Sn_{1-x}Tb_x)Tb_4Rh_6Sn_{18}$ type.[28] Interestingly, among stannides of this series, mainly those containing non-magnetic Sc, Y or Lu attract much attention, which is due to their exciting superconducting properties.[31–37] A further important observation is that such compounds are unknown with Ce, Eu or Yb, which could reveal VF. The only exceptions in this respect would be primitive tetragonal $Yb_{6.6}Ir_6Sn_{16}$,[29] face-centered cubic $Yb_5Pt_6In_{16}Bi_2$ [38] and body-centered tetragonal $Yb_5Ru_6Sn_{18}$ [39] revealing a mixed valence state (*i.e.*, non-integer, but temperature independent) for Yb ions.

Stannides with primitive tetragonal ($a \approx 9.7$ Å, $c \approx 13.7$ Å), face-centered cubic ($a \approx 13.7$ Å) and distorted body-centered cubic ($a \approx 19.4$ Å) structures and compositions close to 3 : 4 : 13 in the Yb–Rh–Sn system were reported to exist by Espinosa.[40] However, in further studies,[41,42] this information has not been confirmed. Furthermore, detailed single-crystal diffraction studies performed on $SnM_3Rh_4Sn_{13}$ (M = La–Gd, Yb, Ca, Sr and Th) explained some earlier observed distortions by anomalous thermal displacements of Sn2-atoms and structural disorder.[43] Finally, a face-centered cubic phase with a unit cell parameter $a \approx 13.7$ Å and the $(Yb_xSn_{1-x})Yb_4Rh_6Sn_{18}$ composition (no refinements were provided) was reported to exist in ref. 44. For unclear reasons, the same work claims Yb atoms to be in an intermediate valence state based on measurements of magnetic susceptibility (not presented) and room-temperature X-ray absorption spectra at the YbL_{III} edge. Considering this information and taking into account unusual valence fluctuations reported for $Yb_3Co_4Ge_{13}$,[45,46] we decided to shed more light on the properties of a stannide with a composition close to the $Yb_3Rh_4Sn_{13}$,[47] recently studied.

In this work, we show that $Yb_5Rh_6Sn_{18}$ crystallizes with a unique structural arrangement, and investigate its magnetic, electrical and thermal transport properties. They reveal a complex temperature-dependent behavior of the Yb ion valence. The observed 'rattling' effect is found to result in a phonon resonance behaviour, resulting in ultra-low thermal conductivity.

2 Experimental

The $Yb_5Rh_6Sn_{18}$ sample of a total mass of 1 g was prepared in a glassy carbon crucible by high-frequency melting from stoichiometric amounts of ytterbium (Ames, 99.95 wt%), rhodium granules (ChemPur, 99.9 wt%), and tin foil (ChemPur, 99.995 wt%). The total weight losses were <0.5 wt%. To avoid oxygen and moisture contaminations, all sample handling and manipulations were performed inside a glove box system under a protective argon atmosphere [$p(H_2O)$, $p(O_2)$ < 1 ppm]. To perform heat treatment, the obtained button was placed in a glassy carbon crucible, sealed in a Ta-tube and enclosed in an evacuated silica ampoule. Further, it was annealed at 1070 K for 720 hours and finally quenched in cold water.

Powder X-ray diffraction (PXRD) was carried out on a Huber G670 Guinier camera (Cu$K_{\alpha1}$ radiation, λ = 1.54056 Å). Phase analysis was performed using the WinXpow software package,[48] and Rietveld refinement using WinCSD.[49] Single-crystal diffraction (SCXRD, two-circle diffractometer Stoe IPDS-2T, Mo$K_{\alpha1}$ radiation, λ = 0.71073 Å) was performed on a crystal mechanically extracted from the crushed sample. The obtained data were refined using the SHELXL-2019/3 program[50] within the WinGX package.[51]

The $Yb_5Rh_6Sn_{18}$ sample was embedded in a conductive resin and polished, and the surface was investigated with a scanning electron microscope (SEM) (Jeol JSM – 7800F) and its chemical composition $Yb_{5.0(1)}Rh_{5.9(1)}Sn_{18.1(1)}$ (in good agreement with the nominal and refined ones) was determined by the mapping procedure with energy dispersive X-ray spectroscopy (EDXS) (Quantax 400 EDXS system, Bruker). Interestingly, in the mapped surface (an area of ≈600 × 600 μm), no traces of Yb_2O_3 were detected (Fig. S1†). This finding confirms, if any, only minor quantities of such an impurity in the studied sample.

The X-ray absorption spectra (XAS) near the YbL_{III} edge of $Yb_5Rh_6Sn_{18}$ were measured in fluorescence mode at 100 K and 293 K at the Rossendorf Beamline (BM20) of ESRF with the help of a Canberra photodiode.[52] The spectra were recorded at a scattering angle of 90° in the horizontal plane.[53] The XAS spectra were recorded in the energy region from 8920 to 9000 eV with a step size of 0.5 eV. The intensity was normalized to the incident flux. The standard normalization routines were applied to the spectra with the help of the PyMCA program.[54]

To investigate the temperature and field dependencies of magnetic susceptibility, specific heat capacity, electrical resistivity, Seebeck coefficient, thermal conductivity and Hall coefficients for $Yb_5Rh_6Sn_{18}$ VSM, ^{4}He heat capacity, TTO and Van der Pauw options of a DynaCool-12 instrument (Quantum Design) were used.

The electronic band structure and density of states were calculated with density functional theory (DFT) [local density approximation (LDA)] using the full-potential FPLO code (version 18.00–52.38).[55] The exchange–correlation potential by Perdew and Wang[56] was used to perform the scalar relativistic calculation. The k-mesh included 8000 points in the first Brillouin zone.

3 Results and discussion

3.1 Crystal structure

The single-crystal XRD (SCXRD) data set of $Yb_5Rh_6Sn_{18}$ was collected from a crystalline shard of an approximate size of 0.01 × 0.02 × 0.03 mm^3. The positions of the strongest reflections were in accordance with a cubic crystal system (*cF*, $a \approx$ 13.8 Å), but additional weak reflections indicated a superstructure (*cP*, $a \approx$ 13.8 Å or *tP*, $a \approx$ 9.7 Å, $c \approx$ 13.8 Å). As the intensities of symmetry-equivalent reflections did not adhere to cubic symmetry (shown in Fig. S2†), it was concluded that the diffraction pattern was produced by a three-domain twin of the tetragonal system with domains of noticeably different diffraction powers. [The twin domains are related to one another by 120° and 240° rotation about [0 1 2]; data of domains 2 and 3 are related to domain 1 according to (−0.5 0.5–0.5) (−0.5 0.5 0.5) (1 1 0) and (−0.5–0.5 0.5) (0.5 0.5 0.5) (−1 1 0), respectively.] For structure solution, the data set of the predominant domain was integrated, and the solution (intrinsic phasing method, ShelXT) was performed with the HKLF4 format data set obtained therefrom. For the final refinement, data integration was performed for all three domains to account for spot shape distortions of the overlapping reflections, and an HKLF5 format data set of all reflections of domain 1 (with overlaps of domains 2 and 3) was created. A numerical absorption correction (cylinder) was applied afterwards in WinGX. In the structure refinement, the population of the twin domains was refined to 0.635(6), 0.293 (6), and 0.072(6) for domains 1, 2 and 3, respectively.

In agreement with the model obtained from the refinement of SCXRD data, all peaks observed in the PXRD pattern of $Yb_5Rh_6Sn_{18}$ could be indexed with the unit cell parameters presented in Table 1 (the difference in the given values obtained from SCXRD is due to diverse methods of their estimation and not due to a negative thermal expansion). The analysis of systematic absences ($h + k = 2n$, $l = 2n$ and $k = 2n$ for *hk*0, *hhl*, 00*l* and 0*k*0, respectively) confirmed the space group (SG) $P4_2/nmc$. Further refinement of atomic coordinates and thermal displacement parameters (Table 2 and 3) converged with low reliability factors (Table 1) confirming its correctness. The obtained profiles are depicted in Fig. 1. Noteworthily, the main peaks in the PXRD pattern of $Yb_5Rh_6Sn_{18}$ could be indexed within a primitive cubic SG $Pm\bar{3}m$ with $a \approx$ 9.8 Å, whereas some of their splittings could be indexed within a primitive tetragonal SG *P*4/*mmm* with unit cell parameters $a \approx c \approx$ 9.8 Å (inset in Fig. 1). These observations suggest a structural relationship of the herein studied phase with the $Yb_3Rh_4Sn_{13}$ Remeika prototype.[21] In this regard, we would like to refer to our previous discussions in ref. 23, 24 and 27.

Interatomic distances in the crystal structure of $Yb_5Rh_6Sn_{18}$ are presented in Table S2.† As for the majority of phases crystallizing in the Remeika type and derived arrangements,[27] there are no Yb–Yb and Rh–Rh bonding contacts (*i.e.*, these distances exceed the $2r\sqrt{2}$ limit, where r_{Yb} = 1.94 Å, r_{Rh} = 1.34 Å and r_{Sn} = 1.41 Å (ref. 57) are atomic radii of the elements) in the herein studied compound. Remarkable shortenings occur in $Yb_5Rh_6Sn_{18}$ for Yb2–2Rh2 (8.0%) and Yb2–1Sn1 (8.5%) distances, whereas the Rh–Sn and Sn–Sn contacts are either slightly shrunk (*e.g.*, Rh1–4Sn4 by 4.0%) or even longer than the corresponding sum (*e.g.*, Sn4–1Sn4 by −2.6%).

Table 1 Crystallographic data collected for $Yb_5Rh_6Sn_{18}$ at different temperatures

Temperature, T (K)	200	293
Method	Single crystal	Powder
Space group (No.)	$P4_2/nmc$ (137)	
Formula per unit cell, Z	2	
Unit cell parameter:		
a (Å)	9.7018(5)	9.6997(4)
c (Å)	13.793(1)	13.7710(7)
V (Å^3)	1298.3(2)	1295.6(2)
Density, ρ (g cm^{-3})	9.26(1)	9.3(1)
Crystal size (mm^3)	0.03 × 0.02 × 0.01	—
Abs. coef., μ (mm^{-1})	38.4	203.3
F(000)	3040	
Radiation	MoK_α	Cu$K_{\alpha1}$
Diffractometer	STOE IPDS 2T	Huber G670
$2\theta_{max}$ (°)	58.0	105.5
$(\sin\theta/\lambda)_{max}$	0.682	0.517
Minimum h, k, l	−13, −13, −18	0, 0, 0
Maximum h, k, l	13, 13, 18	7, 9, 14
Abs. correction	Numerical	—
Collected reflections	14 544	393
Independent reflections	961 (R_{int} = 0.070)	—
Refined parameters	45	31
Refl. with $I_{hkl} \geq 2\sigma(I)$	920 (R_σ = 0.027)	—
Refinement on	F^2	—
R/wR^a; R_I/R_P		0.056/0.121
($I \geq 2\sigma(I)$)	0.042/0.108	
(All data)	0.057/0.116	—
Goodness of fit	1.022	1.011
Min. and max. residual		
Resid. electr. density (e$^-$ Å^{-3})	−2.99; +2.04	−1.12; +1.35

^{a} $w = 1/\sigma^2(F_o)^2 + (0.0757p)^2$ with $p = (F_o^2 + 2F_c^2)/3$.

Table 2 Atomic coordinates and thermal displacement parameters (U_{eq}/U_{iso} × 10^{-3} Å^2) for $Yb_5Rh_6Sn_{18}$

Atom	Site	x	y	z	U_{eq}/U_{iso}
200 K					
Yb1	2*b*	3/4	1/4	1/4	21.0(4)
Yb2	8*g*	1/4	0.0255(1)	0.38263(8)	19.4(2)
Rh1	4*c*	3/4	1/4	0.5060(2)	15.8(6)
Rh2	8*f*	0.4953(1)	−*x* + 1	1/4	17.2(4)
Sn1	4*d*	1/4	1/4	0.0389(2)	27.5(1)
Sn2	8*g*	1/4	0.0999(1)	0.7388(2)	21.6(4)
Sn3	8*g*	1/4	0.5787(2)	0.1634(1)	19.6(3)
Sn4	16*h*	0.5758(2)	0.0743(1)	0.0737(1)	22.9(3)
293 K					
Yb1	2*b*	3/4	1/4	1/4	29(6)
Yb2	8*g*	1/4	0.0229(9)	0.3826(7)	31(4)
Rh1	4*c*	1/4	1/4	0.5069(9)	26(9)
Rh2	8*f*	0.4970(9)	−*x* + 1	1/4	26(6)
Sn1	4*d*	1/4	1/4	0.0354(9)	39(7)
Sn2	8*g*	1/4	0.0991(9)	0.7404(9)	20(6)
Sn3	8*g*	1/4	0.5743(9)	0.1643(9)	29(5)
Sn4	16*h*	0.5737(9)	0.0744(9)	0.0739(9)	26(3)

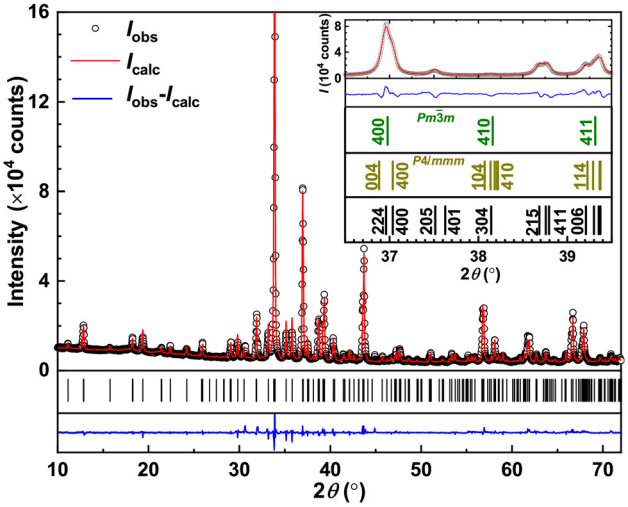

Fig. 1 Powder X-ray diffraction patterns of $Yb_5Rh_6Sn_{18}$. Inset: selected range of PXRD patterns with possible indexing within cubic (SG $Pm\bar{3}m$, $a \approx 9.8$ Å), tetragonal (SG $P4/mmm$, $a \approx c \approx 9.8$ Å) and the model (SG $P4_2/nmc$) refined in this work.

Table 3 Anisotropic thermal displacement parameters (U_{ij} × 10^{-3} Å^2) for $Yb_5Rh_6Sn_{18}$

Atom	U_{11}	U_{22}	U_{33}	U_{12}	U_{13}	U_{23}
Yb1	20.2(7)	U_{11}	23(1)	0	0	0
Yb2	18.4(5)	19.9(5)	U_{22}	0	−0.1(4)	0
Rh1	14(1)	16(1)	18(2)	0	0	0
Rh2	16.9(6)	U_{11}	18(1)	−0.4(4)	U_{12}	0.0(8)
Sn1	24(1)	41(1)	18(1)	0	0	0
Sn2	15.5(9)	17.6(9)	31.6(9)	−0.9(6)	0	0
Sn3	16.4(7)	21.1(7)	21.5(8)	3.2(6)	0	0
Sn4	26.0(6)	23.1(6)	19.6(8)	1.9(4)	−0.4(4)	−8.9(5)

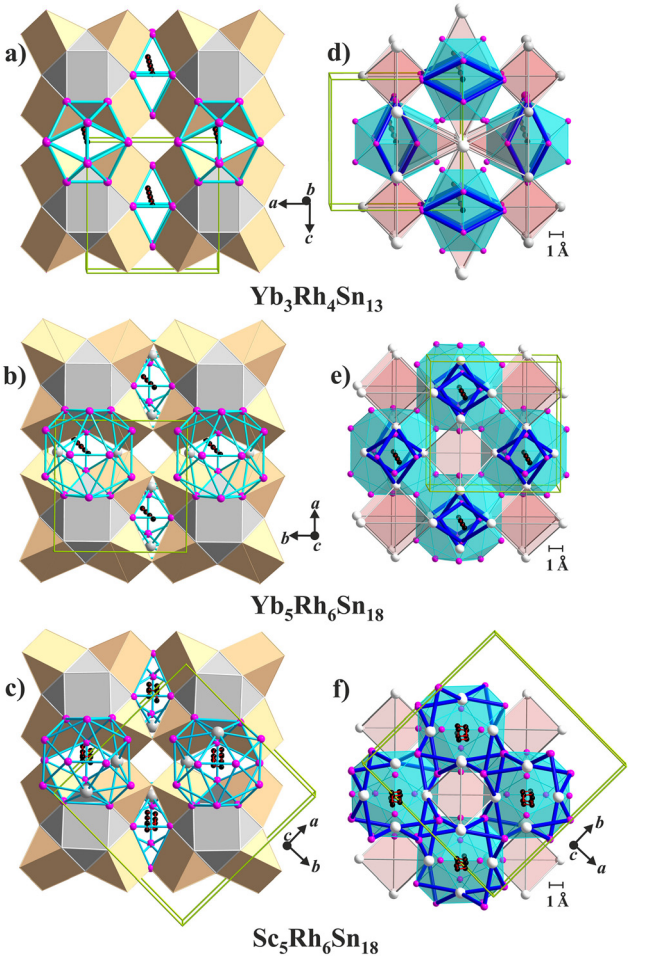

Fig. 2 Packing of [$RhSn_6$] trigonal prisms (tan), [$YbSn_{12}$] cuboctahedra together with [$SnSn_{12}$] icosahedra (gray) and 16-vertices distorted Frank–Kasper [SnM_2Sn_{14}] (M = Sc and Yb) polyhedra (cyan) in the structures of $Yb_3Rh_4Sn_{13}$ (a), $Yb_5Rh_6Sn_{18}$ (b) and $Sc_5Rh_6Sn_{18}$ (c). [Yb_4] tetrahedra together with tetragonal fragments [Sn_4] within the icosahedra (d) and [M_2Sn_2] within the Frank–Kasper polyhedra (e and f) are given in red and thick blue lines, respectively. Yb and Sn atoms at the vertices of polyhedra are depicted as magenta and white balls, whereas Sn atoms centering them are depicted as black balls.

Having a stoichiometry 5 : 6 : 18, the compound studied here is expected to be structurally related to the series of $M_5Rh_6Sn_{18}$ (M = Y, Tb, Dy, Ho, Er, and Tm) stannides crystallizing with the $(Sn_{1-x}Tb_x)Tb_4Rh_6Sn_{18}$ type (SG $I4_1/acd$, $a_{tetr} \approx 13.8$ Å, $c_{tetr} \approx 27.5$ Å),[58] which is considered to be a derivative of the $Yb_3Rh_4Sn_{13}$ Remeika prototype (SG $Pm\bar{3}m$, $a_{cub} \approx 9.7$ Å). Indeed, comparing the unit cell parameters from Table 1 with the abovementioned observations, clear relations become visible: $a \approx a_{cub} \approx a_{tetr}/\sqrt{2}$ and $c \approx a_{cub}\sqrt{2} \approx c_{tetr}/2$. Such a close relationship between UCPs is also reflected in the structural arrangements. As one can see from Fig. 2a, b and c, in all three types [for better visualization, we present $Sc_5Rh_6Sn_{18}$ in Fig. 2c, which is an ordered variant of the $(Sn_{1-x}Tb_x)Tb_4Rh_6Sn_{18}$ type], an array of corner sharing [$RhSn_6$] trigonal prisms (tan) with [$YbSn_{12}$] cuboctahedra (gray) incorporated into the free space in-between occurs. In the case of the cubic $Yb_3Rh_4Sn_{13}$ prototype, trigonal faces of prisms and cuboctahedra are shared with those of [$SnSn_{12}$] icosahedra (cyan) (Fig. 2a), whereas for the tetragonally distorted 5 : 6 : 18 variants (Fig. 2b and c), the 16-vertices distorted Frank–Kasper [SnR_2Sn_{14}] polyhedra share these with only cuboctahedra. Additionally, the latter units in $Sc_5Rh_6Sn_{18}$ are distorted in a different way due to diverse distributions of M atoms therein (Fig. 2c), which results in the shifted positions of centering Sn atoms (black connected with red zigzag). On the other hand, in the structures of $Yb_3Rh_4Sn_{13}$ (Fig. 2a) and $Yb_5Rh_6Sn_{18}$ (Fig. 2b), the Sn atoms centering the similar voids are along a straight line (red).

In Fig. 2d, e and f, we demonstrate the packing of [Yb_4] tetrahedra (red) together with tetrahedral fragments (marked with thick blue lines) within the [$SnSn_{12}$] icosahedra and 16-vertices distorted Frank–Kasper [SnM_2Sn_{14}] polyhedra (both units are given in cyan). These fragments consist of only Sn atoms in the case of $Yb_3Rh_4Sn_{13}$ (Fig. 2d), whereas for $Yb_5Rh_6Sn_{18}$ (Fig. 2e) and $Sc_5Rh_6Sn_{18}$ (Fig. 2f), they contain 2Sn and 2M. Again, being nearly equally oriented in Yb-containing

stannides, they reveal different distributions in the $Sc_5Rh_6Sn_{18}$ type.

Similarly to $Yb_5Rh_6Sn_{18}$, $Yb_{6.6}Ir_6Sn_{16}$ crystallizes with the same space group, close unit cell parameters and even identical Wyckoff positions.[29] The only difference between these structural arrangements is the appearance of an 8*g* site occupied by Yb (≈40%) in the Ir-containing stannide instead of Sn1 at the 4d position (Table 2), which results in various compositions.

All these let us to conclude that $Yb_5Rh_6Sn_{18}$ crystallizes with a unique structural arrangement, which belongs to the family of derivatives of the $Yb_3Rh_4Sn_{13}$ Remeika prototype.

3.2 X-ray absorption spectroscopy

The X-ray absorption spectra (XAS) of $Yb_5Rh_6Sn_{18}$ measured at the YbL_{III} edge are presented in Fig. 3. They reveal two white lines, which are attributed to Yb-4f^{14} (≈8940.5 eV) and Yb-4f^{13} (≈8946 eV) configurations, respectively. Interestingly, the XAS measured here at room temperature are nearly identical to those reported for a $(Yb_xSn_{1-x})Yb_4Rh_6Sn_{18}$ compound, which was believed to crystallize with the face-centered cubic structure (SG $Fm\bar{3}m$, a = 13.74 Å).[44]

A clear reduction of the intensity of the low-energy line (≈8940.5 eV) in the XAS of $Yb_5Rh_6Sn_{18}$ with increasing temperature is observed. This is an indication of the fluctuating valence [*i.e.* intermediate valence state (IVS)] of ytterbium. Indeed, by deconvoluting the measured spectra, we obtain $Yb^{2.59(1)+}$ and $Yb^{2.62(1)+}$ at 100 K and 293 K, respectively. Interestingly, similar valence evolution is reported for the $Yb_3Co_4Ge_{13}$ modulated Remeika phase[46] and $YbPtGe_2$: a multivalent charge-ordered system with an unusual spin pseudogap.[59] The IVS in $Yb_5Rh_6Sn_{18}$ is in contrast with the prevailing temperature-independent state of Yb-4f^{14} (*i.e.*, Yb^{2+}) observed in the weakly Pauli paramagnetic and superconducting $Yb_3Rh_4Sn_{13}$ compound with a close composition.[44,47]

Furthermore, we compared the Yb-5d electronic density of states (DOS) obtained from the theoretical DFT calculations with the measured XAS. They are expected to reproduce the lower-energy feature in the spectra and therefore became shifted to ≈8940.5 eV. As one can see from Fig. 3, the Yb1-5d orbitals are mainly unoccupied (they are above the Fermi level E_F) and nicely coincide with the position of the corresponding absorption maximum. However, unexpectedly, the 5d states of the Yb2 atom are found to be partially occupied. Also, these orbitals contribute remarkably to the higher-energy absorption maximum at ≈8946 eV corresponding to the Yb-4f^{13} configuration, which would assume an underestimation of the Yb^{2+} fraction in the valences obtained from the deconvolution of XAS. Since the temperature dependence of the Yb2-5d DOS cannot be simulated, its influence on the IVS behavior in $Yb_5Rh_6Sn_{18}$ remains rather unclear.

3.3 Magnetic susceptibility

Temperature dependence of magnetic susceptibility [$\chi(T)$] for $Yb_5Rh_6Sn_{18}$ is depicted in Fig. 4. It obeys the Curie–Weiss (CW) law for 180 K < T < 350 K (inset in Fig. 4). The effective magnetic moment μ_{eff} = 2.94(5)μ_B deduced from such a fit is approximately by a factor of 3/2 smaller than 4.54μ_B – a value theoretically calculated for the Yb-4f^{13} configuration. A similar situation was observed in $YbPtGe_2$, where the Yb atom in one of the crystallographic positions was shown to be non-magnetic (*i.e.*, in the Yb-4f^{14} state),[59,60] which resulted in the reduction of μ_{eff} by a factor of ≈ $\sqrt{2}$. Also, the performed CW fit indicated a large negative Weiss temperature of Θ_P = −175 (1) K, which can be explained by an enhanced characteristic energy (≈47 K) of valence fluctuations.

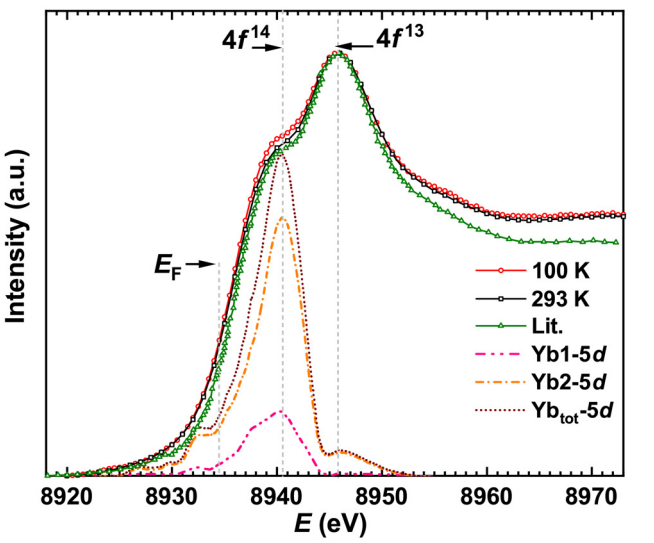

Fig. 3 Temperature-dependent X-ray absorption spectra of $Yb_5Rh_6Sn_{18}$ at the YbL_{III} edge in comparison with the literature data for $(Yb_xSn_{1-x})Yb_4Rh_6Sn_{18}$ [44] and the theoretically calculated Yb-5d density of states.

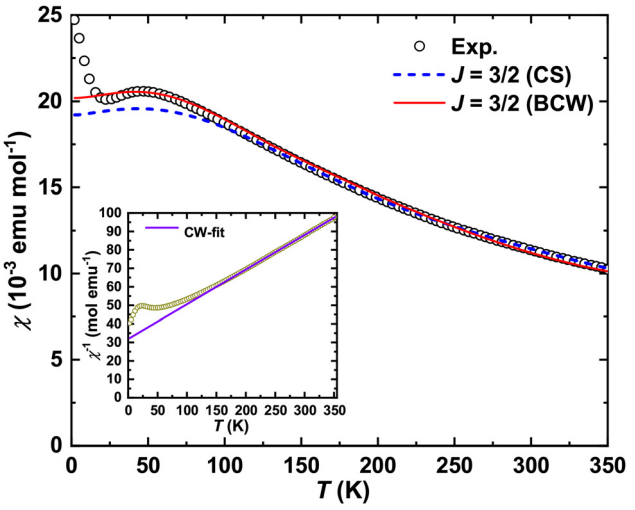

Fig. 4 Temperature dependence of magnetic susceptibility (μ_0H = 7 T) for $Yb_5Rh_6Sn_{18}$ together with the predictions of the Coqblin–Schrieffer (CS) and Bickers–Cox–Wilkins (BCW) models for the J = 3/2 multiplet. Insets: temperature dependence of the reciprocal magnetic susceptibility of $Yb_5Rh_6Sn_{18}$ together with the Curie–Weiss (CW) fit.

Below 180 K, the $\chi(T)$ of $Yb_5Rh_6Sn_{18}$ deviates from the CW law, overcomes a maximum centered at $T_{max}^{\chi} \approx 47$ K and finally reveals an upturn for $T < 25$ K (Fig. 4) due to a minor (invisible in XRD) paramagnetic impurity. Such a behavior of magnetic susceptibility is in line with the IVS observed in XAS. Noteworthily, T_{max}^{χ} varies in a broad range for Yb-containing intermetallics, revealing the IVS [*e.g.*, 25 K for $YbPd_2Si_2$,[20] 30 K for YbCuAl,[18] 150 K for $Yb_3Co_4Ge_{13}$,[46] 240 K for Yb_4Sb_3,[61] 250 K for $YbNi_{0.8}Al_{4.2}$,[62] 250 K for $YbPtGe_2$,[59] 400 K for $YbNiAl_4$,[63] 500 K for Yb_3Ge_5,[64] *etc.*]. Such a behavior is expected to be universally described by a Coqblin–Schrieffer (CS) model proposed by Rajan for the whole Yb^{3+} multiplet $J = 7/2$ (*i.e.*, degeneracy $N = 2J + 1 = 8$).[13] However, since this model does not account for crystal electric field (CEF) effects, the low temperature lattice problem and the so-called Kondo limit (*i.e.*, valence variation, $0.5 < n_f < 1$), it frequently fails in the description of the IVS, as it is the case for *e.g.*, $YbPd_2Si_2$,[20] YbCuAl,[18] $Yb_3Co_4Ge_{13}$,[46] *etc.*

A similar observation is made for the herein studied $Yb_5Rh_6Sn_{18}$, where a good description for $T > 100$ K is obtained with $J = 3/2$ ($N = 4$) and the characteristic spin-fluctuation temperature $T_0 = 201$ K. The situation can be somewhat improved while switching to the Anderson model developed for the same multiplet and $n_f = 1$ by Bickers, Cox and Wilkins (BCW)[9] (Fig. 4). From such a fit, we obtained a similar characteristic temperature $T_0 = 208$ K. Using the Rajan prediction[13] for the Sommerfeld coefficient of electronic specific heat, we calculated $\gamma = 2J\pi k_B N_A/6T_0 \approx 63$ mJ mol^{-1} K^{-2} (with $k_B = 1.38 \times 10^{-23}$ J K^{-1} and $N_A = 6.022 \times 10^{-23}$ mol^{-1} as Boltzmann and Avogadro constants, respectively) – a value that seems to be degeneracy-independent and would even be in fair agreement with the corresponding value obtained from c_p-measurements (see below). However, implying the obtained T_0 to be correct, we calculated a Kondo temperature: $T_K = 2\pi T_0 W_J(2J + 1)^{-1} \approx 191$ K (where $W_{3/2} = 0.5843$ is the Wilson number),[65] which is in complete disagreement with the measured electrical resistivity, revealing no signature of any Kondo-like behavior at this T_K.

In view of the complicated Yb valency situation (*i.e.*, Yb2-5d states contribute to the Yb^{3+} fraction), it is not surprising that the classical CS and BCW models do not work well. Additionally, as it is shown in section 1.1 and Fig. S3 of the ESI,† the simplified two-level interconfigurational fluctuation model (ICF)[66] fails in the description of the valence fluctuations in $Yb_5Rh_6Sn_{18}$ as well, thus confirming the conclusion above.

3.4 Specific heat

The temperature dependence of specific heat capacity $c_p(T)$ of $Yb_5Rh_6Sn_{18}$ reveals no anomalies for 3 K < T < 200 K (inset in Fig. 5) and reaches the Dulong–Petit limit $c_p = 3nR \approx 723$ J mol^{-1} K^{-1} ($R = 8.31$ J K^{-1} mol^{-1} is the gas constant) at ≈183 K. However, it reveals an anomaly at $T_N = 2.3$ K (Fig. S4†). This is due to a minor (not detectable with XRD or EDX) Yb_2O_3 impurity ordering antiferromagnetically.[67] The influence of such an impurity on the physical properties of the similar $Yb_3Pt_4Ge_{13}$ is discussed in detail in ref. 22. Noteworthily, the cusp at the transition in the current case is by a factor of ≈3 smaller than that in ref. 22. Therefore, we further consider the specific heat of $Yb_5Rh_6Sn_{18}$ in the $c_p/T(T^2)$ presentation and assume it to follow an *ansatz* of $c_p = \gamma T + \beta T^3$ in a temperature range of ≈4.5–6.1 K (Fig. S4†). This would indicate $\gamma \approx 55(5)$ mJ mol^{-1} K^{-2} and $\Theta_D = 148(2)$ K – values that are very similar to those reported for non-magnetic $Sc_5Rh_6Sn_{18}$ [34] and $Lu_5Rh_6Sn_{18}$.[68]

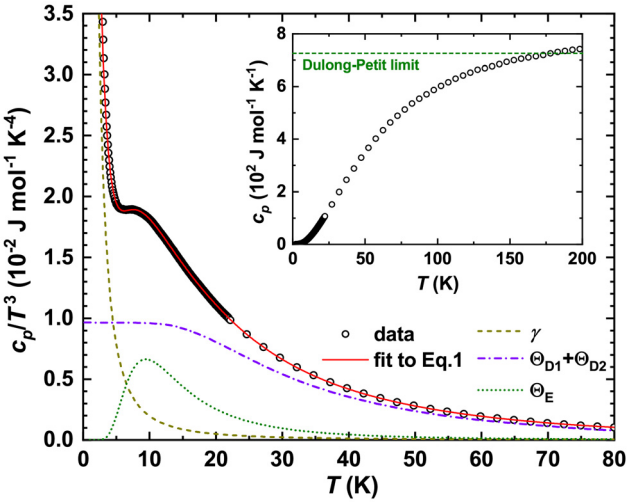

Fig. 5 Specific heat for $Yb_5Rh_6Sn_{18}$ in the $c_p/T^3(T)$ presentation together with a fit to eqn (1) and Debye (Θ_{D1} + Θ_{D2}), Einstein (Θ_E) and electronic (γ) contributions. Inset: specific heat for $Yb_5Rh_6Sn_{18}$.

For $T > 6$ K, the $c_p(T)$ of $Yb_5Rh_6Sn_{18}$ deviates from the above given *ansatz*, which is confirmed by a well-pronounced maximum centered at ≈8 K observed for the $c_p/T^3(T)$ presentation (Fig. 5). It signals a contribution of low energy Einstein optical modes to the measured specific heat. One of the possible reasons of their appearance could be the so-called 'rattling' motion[69] of Sn1 atoms within the enlarged 16-vertices distorted Frank–Kasper polyhedra (Fig. 2b). Such an effect is discussed for some Remeika phases.[27] To describe it, a combined Debye–Einstein model is frequently used.[70,71] It assumes as a first approximation[72] the separation of phononic contributions originating from different types of sublattices (*i.e.*, covalently and ionically bonded) and is given as follows:

$$c_p T^{-3}(T) = \sum_i c_{Di} T^{-3}(T) + \sum_j c_{Ej} T^{-3}(T) + \gamma T^{-2} \quad (1)$$

where the Debye contribution is given as:

$$c_{Di}(T) = 3N_{Di}R\left(\frac{T}{\Theta_{Di}}\right)^3 \int_0^{\Theta_{Di}/T} \frac{x^4 e^x}{(e^x - 1)^2} dx \quad (2)$$

(with $x = \hbar\omega/k_B T$) and the Einstein one as:

$$c_{Ej}(T) = N_{Ej}R\left(\frac{\Theta_{Ej}}{T}\right)^2 \frac{e^{\Theta_{Ej}/T}}{(e^{\Theta_{Ej}/T} - 1)^2} \quad (3)$$

By fitting the $c_p(T)$ of $Yb_5Rh_6Sn_{18}$ to eqn (1), the characteristic Debye and Einstein temperatures and number of modes

were found to be Θ_{D1} = 300(2) K, Θ_{D2} = 134(2) K, and Θ_{E1} = 47 (1) K and N_{D1} = 59(1), N_{D2} = 30(1), and N_{E1} = 4(1), respectively. Comparing this result with the $Yb_5Rh_6Sn_{17}Sn_1$ (Sn1 should remain for a possible 'rattling') stoichiometry, N_{D1} could be assumed to originate mainly from the covalently bonded Sn_{17} framework (*i.e.*, theoretically expected number of Debye modes is 51). N_{D2} is then due to 5Yb and 6Rh atoms (theoretical value of 33) and finally N_{E1} is from 1Sn1 in the enlarged [Sn1M_2Sn$_{14}$] polyhedron (should be 3). In total, the abovementioned stoichiometry indicates 87 possible modes, whereas our fit results in $N_{tot} = N_{Di} + N_{Ej}$ = 93(1). The mismatches between the theoretical expectations and the experiment are not a rare case (here we would like to refer to ref. 47, 71, 73 and 74) and reflect the shortcomings of the simple model applied to the complex phononic spectra of compounds.

Interestingly, taking the thermal displacement parameter $B_{iso} = 8\pi^2 U_{iso}$ = 3.1(1) Å^2 of the 'rattling' Sn1 atom refined from the powder XRD data at room temperature (Table 2) and implementing it into eqn (4), we obtained the Einstein temperature Θ_E^B = 55(1) K, which fairly agrees with the specific heat data. This is a rather unexpected result. As it has been shown for such well-established 'rattling' systems as filled skutterudites[75,76] and the recently studied $Yb_3Rh_4Sn_{13}$,[47] if the atomic masses of the 'rattling' systems are comparable with those of the atoms forming the framework, Θ_E and Θ_E^B differ strongly.

$$\Theta_E^B = \sqrt{\frac{8\pi^2\hbar^2 T}{m_{Sn} k_B B_{eq}}} \quad (4)$$

(where $\hbar = 1.055 \times 10^{-34}$ J s is a Dirac constant).

The fit to eqn (1) also resulted in an enhanced Sommerfeld coefficient of the electronic specific heat γ = 196(1) mJ mol^{-1} K^{-2}, which is by a factor of ≈4 larger than the values observed from the classical *ansatz* as well as for the non-magnetic $Sc_5Rh_6Sn_{18}$ [34] or $Lu_5Rh_6Sn_{18}$.[68] This is again due to the enhancement of low-temperature $c_p(T)$ caused by the Yb_2O_3 impurity.

3.5 Electrical transport

The temperature dependence of electrical resistivity $\rho(T)$ for $Yb_5Rh_6Sn_{18}$ is presented in Fig. 6. In contrast to that for $Lu_5Rh_6Sn_{18}$ – a phonon reference compound[77] – as well as $Y_5Rh_6Sn_{18}$,[78] $Sc_5Rh_6Sn_{18}$,[34,35] $Y_5Ir_6Sn_{18}$,[30] analogous intermetallics, *etc.*, it increases with increasing temperature and is of the same order of magnitude as that of a metal.[79] Furthermore, in the temperature range of ≈4–12 K, $\rho(T)$ of $Yb_5Rh_6Sn_{18}$ follows the Fermi-liquid behavior and fits well to $\rho_0 + A_{FL}T^2$, with ρ_0 = 61(1) μΩ cm and A_{FL} = 0.13(1) μΩ cm K^{-2}. However, this $\rho(T)$ cannot be described by a Bloch–Grüneisen model (typical of metals)[80] in the whole temperature range (for more details, see the discussions in section 1.2 of the ESI†), which is most probably due to the change of the scattering mechanism at $T \approx 100$ K. Similar temperature dependencies of electrical resistivity were reported for such unusual IVS as $CePt_4Ge_{12}$ [81] and $YbPtGe_2$.[59]

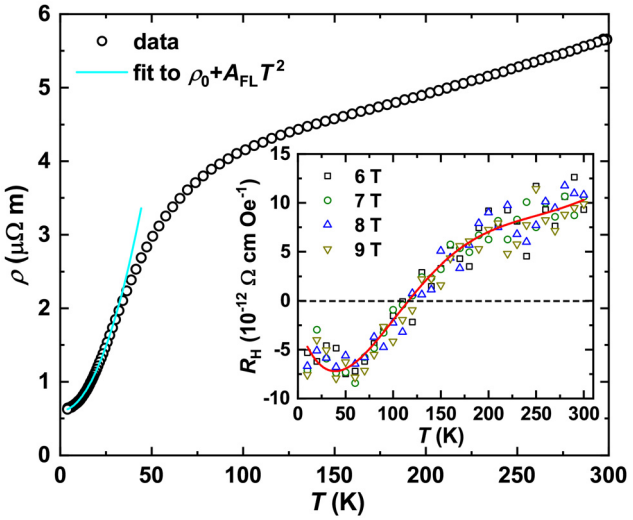

Fig. 6 Temperature dependence of electrical resistivity $\rho(T)$ for $Yb_5Rh_6Sn_{18}$ together with the fit to the Fermi-liquid model. Inset: temperature dependence of the Hall coefficient $R_H(T)$ for $Yb_5Rh_6Sn_{18}$ in different magnetic fields. The red line is a guide for the eye only.

Taking the values obtained from the Fermi-liquid fit, we estimated the residual resistance ratio RRR = $\rho_{(300)}/\rho_0 \approx 9.3$, which indicates a fair quality of the studied sample. From the quadratic term, Kadowaki–Woods ratios[82] ($R_{KW} = A_{FL}/\gamma^2$) of 4.2 × 10^{-5} μΩ cm (mol K mJ^{-1})^2 [for $\gamma \approx$ 55(5) mJ mol^{-1} K^{-2}] and 3.4 × 10^{-6} μΩ cm (mol K mJ^{-1})^2 [for $\gamma \approx$ 196(1) mJ mol^{-1} K^{-2}] were obtained. Both the obtained values differ strongly from the R_{KW} = 1.0 × 10^{-5} μΩ cm (mol K mJ^{-1})^2 expected for a heavy fermion compound, which is in line with the IVS of $Yb_5Rh_6Sn_{18}$.

Temperature dependence of the Hall coefficient $R_H(T)$ for $Yb_5Rh_6Sn_{18}$ in different magnetic fields is presented in the inset of Fig. 6. Being nearly field independent, $R_H(T)$ mimics the behavior of the Seebeck coefficient (see below, Fig. 7), revealing a well-pronounced minimum at $T_{min}^{R_H} \approx 50$ K and changing the sign from negative to positive at $T \approx 120$ K. This latter observation confirms the switching of the conduction mechanism from electron- to hole-like type. By applying the one-band model [$R_H = (n|e|)^{-1}$ and $\mu = R_H/\rho$], we found that their charge carrier concentration n and mobility μ vary (with the exception of singularity at R_H = 0) in the narrow ranges of 7.6–9.4 × 10^{-21} cm^{-3} and 1.1–2.1 cm^2 V^{-1} s^{-1}, respectively. Weak temperature dependence of both these characteristics and their order of magnitudes indicate $Yb_5Rh_6Sn_{18}$ to be a metal.[79] By further applying the free electron gas model, we calculated the Fermi energy $E_F = (\hbar^2/2m)(3\pi^2 n)^{2/3} e^{-1}$ = 1.52(9) eV and the DOS at the Fermi level $D(E_F) = 3nV/2E_F$ = 10.9(4) states eV^{-1} f.u.$^{-1}$. The latter value is strongly underestimated in comparison with the theoretically calculated one, which is in line with a complex electronic band structure of $Yb_5Rh_6Sn_{18}$ (see the discussion below).

Temperature dependence of the Seebeck coefficient of thermopower $S(T)$ for $Yb_5Rh_6Sn_{18}$ in logarithmic and linear scales is shown in Fig. 7 and the inset therein, respectively. It is negative

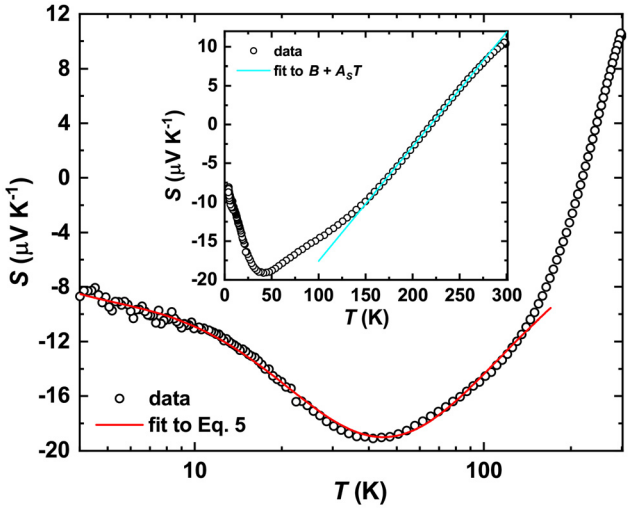

Fig. 7 Temperature dependence of the Seebeck coefficient $S(T)$ for $Yb_5Rh_6Sn_{18}$ on a logarithmic scale together with the fit to eqn (5). Inset: temperature dependence of the Seebeck coefficient $S(T)$ for $Yb_5Rh_6Sn_{18}$ on a linear scale together with the linear fit as expected for a metallic system.

in the LT range and decreases with increasing temperature, passing through a minimum centered at $T^{S}_{min} \approx 41$ K (in fair agreement with T^{χ}_{max}). Furthermore, $S(T)$ starts to increase steeply, becoming almost linear, and changes the sign to positive at $T \approx 220$ K, which indicates the switch from n- to p-type conductivity.

Having two crystallographic positions for Yb atoms in the structure of $Yb_5Rh_6Sn_{18}$, we assumed that the conduction electrons scattered on two independent 4f quasiparticle bands. This prompted us to try to describe $S(T)$ using the model proposed by Bando *et al.*:[83]

$$S(T) = \frac{A_N T}{B_N^2 + T^2} + \frac{A_W T}{B_W^2 + T^2} \quad (5)$$

with

$$A_{N,W} = \frac{2\Delta_{N,W}}{|e|};\ B^2 = 3\frac{\Delta_{N,W}^2 + \Gamma_{N,W}^2}{\pi^2 k_B^2} \quad (6)$$

where $\Delta_{N,W} = \varepsilon_{N,W} - \varepsilon_F$ and $\Gamma_{N,W}$ are the position relative to the Fermi level and half width of the band, respectively. Hence, the corresponding Lorentzian density of states is expressed as:

$$N^{4f}_{N,W} = \frac{W}{\pi}\frac{\frac{1}{2}\Gamma}{(\varepsilon_{N,W} - \varepsilon)^2 + (12\Gamma)^2} \quad (7)$$

Here, $W = Q^{+}z + Q^{-}(1 - z)$ is the integrated weight approximated for the intermediate valence regime with $Q^{+} = N$ (*i.e.*, the degeneracy of Yb ions), $Q^{-} = 1$ and the number of holes in the 4f-shell is estimated as $n_h = 1 - z$.[84] The latter value can also be derived from:

$$n_h = 1 - z = \int_{\varepsilon_F}^{\infty} N^{4f}(\varepsilon)\mathrm{d}\varepsilon \quad (8)$$

The parameters obtained from the fit of $S(T)$ of $Yb_5Rh_6Sn_{18}$ to eqn (5) and the theory related to it are presented in Table 4. Knowing that the Yb valence is given as $\nu = 3 - z$, we can state that from these calculations, it is ≈2.9 for both bands if one assumes the whole $J = 7/2$ ($N = 8$) multiplet for Yb ions. These values strongly deviate from those observed experimentally from XAS and can become somewhat improved (*i.e.*, to ≈2.8) while taking into consideration the $J = 3/2$ ($N = 4$) multiplet applied for the description of temperature dependence of magnetic susceptibility. Such an inconsistency can be explained by the fact that the applied model is much too simple, which stresses again the fact that the Yb valence fluctuation in the studied stannide is of a very complex mechanism. Interestingly, the Yb-valences obtained here are in good agreement with those deduced from the ICF fit to the magnetic susceptibility of $Yb_5Rh_6Sn_{18}$. With due caution, we thus conclude that the simplifications in both theories (*i.e.*, electron scattering on two quasiparticle bands and valence fluctuations between two energetic levels, respectively) result in comparable values.

In the temperature range of 150–250 K, the Seebeck coefficient of $Yb_5Rh_6Sn_{18}$ fits well to $S(T) = A_S T + B$ (the inset in Fig. 7) with the carriers' diffusion component $A_S = \pi^2 k_B^2/2eE_F = 0.15(1)$ μV K^{-2} and the term due to the contribution of electronic interaction $B = -32(1)$ μV K^{-2}.[85,86] Having these fit parameters, we calculated the Fermi energy $E_F = 1.64(9)$ eV, which is in good agreement with the value obtained from Hall effect measurements.

3.6 Thermal conductivity

The temperature dependence of the thermal conductivity $[\kappa_{tot}(T)]$ of $Yb_5Rh_6Sn_{18}$ is depicted in Fig. 8. It is very low and thus comparable with those of such well-established 'rattling' systems as intermetallic clathrates[87–89] and filled skutterudites.[90] To shed light on this behavior, we decomposed $\kappa_{tot}(T)$ into its electronic ($\kappa_{el} = [L(T)/\rho(T)]T$) and phononic ($\kappa_{ph} = \kappa_{tot} - \kappa_{el}$) parts. Knowing that the Lorenz number $L_0 = 2.44 \times 10^{-8}$ W Ω K^{-2} is temperature dependent, we corrected it as proposed in:[91]

$$L(T) = 1.5 + \exp\left(-\frac{|S(T)|}{116}\right) \quad (9)$$

[in this equation, $|S(T)|$ is given in μV K^{-1} and $L(T)$ is given in 10^{-8} W Ω K^{-2}].

As one can see from Fig. 8, the phononic contribution to the thermal conductivity of $Yb_5Rh_6Sn_{18}$ is larger than the electronic one, which is again similar to the situation in the above-

Table 4 Positions (Δ) and half-widths (Γ) of 4f quasiparticle bands in $Yb_5Rh_6Sn_{18}$ derived from the temperature dependence of the Seebeck coefficient and assuming different degeneracies (N) for Yb ions

i	Δ_i (meV)	Γ_i (meV)	z ($N = 8$)	z ($N = 4$)
N	−0.86(5)	7.30(5)	0.09(1)	0.15(1)
W	−0.02(1)	0.56(1)	0.10(1)	0.19(1)

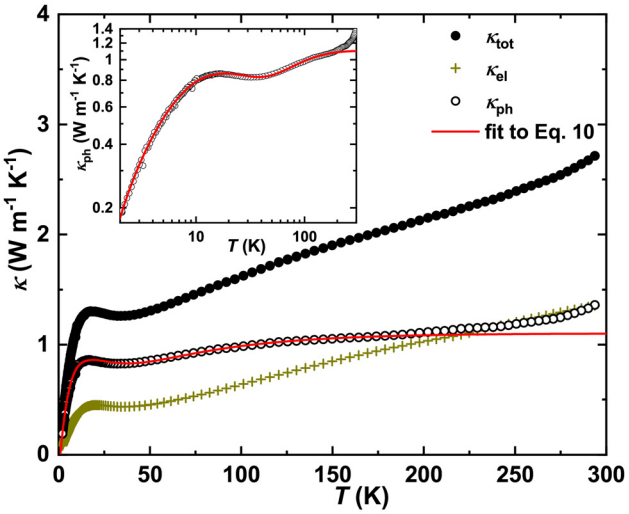

Fig. 8 Temperature dependence of thermal conductivity and its electronic κ_{el} and phononic κ_{ph} contributions for $Yb_5Rh_6Sn_{18}$ together with the fit to eqn (10). For $T > 250$ K, $\kappa_{tot}(T)$ and κ_{ph} reveal an upturn following the $\propto T^3$ law due to radiation heat losses. Inset: κ_{ph} together with the fit to eqn (10) on a logarithmic scale for the better visualization of a minimum at $T_{min} \approx 40$ K.

mentioned 'rattling' systems. Furthermore, the obtained $\kappa_{ph}(T)$ reveals a well-pronounced minimum at $T_{min} \approx 40$ K (inset in Fig. 8), which could be a signature of the so-called phonon resonance (PR).[92] There are two known reasons for the appearance of such a phenomenon: (i) resonant interaction occurring between phonons and non-paramagnetic lattice point defects (reported for mixed halides[93,94] and recently for natural galena[95]) and/or (ii) anticipated scattering of the phonons by the vibrations of a weakly bound cation incorporated inside an enlarged anionic void (*i.e.*, 'rattling' effect).[96] The modified Debye–Callaway model[97] [eqn (10)] allows accounting for different scattering mechanisms of phonons (including PR) and to describe $\kappa_{ph}(T)$.

$$\kappa_{ph} = \frac{k_B{}^4 T^3}{2\pi^2 v_S \hbar^3} \int_0^{\Theta_D/T} \frac{1}{\tau_{tot}^{-1}} \frac{x^4 e^x}{(e^x - 1)^2} dx \qquad (10)$$

In eqn (10), we used $\Theta_D = 148(2)$ K, the average sound velocity $v_S = k_B\Theta_D/h(6\pi^2 n_{at})^{1/3} = 1435(1)$ m s^{-1} (with the concentration of atoms per unit cell volume $n_{at} = 4.48 \times 10^{28}$ m^{-3}) deduced from XRD refinement and $x = \hbar\omega/k_BT$. The total relaxation time τ_{tot}^{-1} in the current case includes the following contributions: phonon scattering on (i) grain boundaries (τ_B^{-1}) and (ii) point defects (τ_{PD}^{-1}), (iii) normal (τ_N^{-1}) and (iv) *umklapp* (τ_U^{-1}) phonon processes and (v) τ_{PR}^{-1} due to phonon resonance:

$$\tau_{tot}^{-1} = \tau_B^{-1} + \tau_{PD}^{-1} + \tau_N^{-1} + \tau_U^{-1} + \tau_{PR}^{-1} \qquad (11)$$

with

$$\tau_{PR}^{-1} = \frac{C_5\omega^2}{[(\omega_{PR}^2 - \omega^2)^2 + (C_6/\pi)^2\omega^2\omega_{PR}^2]} \qquad (12)$$

Parameters obtained from the fit to eqn (10) are presented in Table 5. Interestingly, the observed C_1 value is by 1–2 orders of magnitude smaller than those reported for the intermetallic ErPdSb[98] or semiconducting PbS[95] and $In_{1-y}@_yIn_2S_4$[74] thermoelectric materials. This means that phonon scattering on the grain boundaries in $Yb_5Rh_6Sn_{18}$ is rather weak. On the other hand, parameter C_2, which is due to the point defects, is (for the stannide studied here) by a factor of 10–100 larger than the analogues in the abovementioned compounds. Thus, this scattering process is a dominating one in the low temperature regime. For $T > 50$ K, the dominance of normal and umklapp phonon–phonon processes is observed, which is reflected in the remarkable C_3 and C_4 parameters. Such a clear separation of both contributions is frequently not the case, especially for intermetallic systems. For instance, the normal processes seem to be completely screened by the umklapp ones in ErPdSb[98] and as a result, no C_3 parameter is obtained from the fit to the Debye–Callaway model. In concluding this discussion, we emphasize that the C_{1-4} parameters obtained for $Yb_5Rh_6Sn_{18}$ are quite conventional and do not provide any insights into the ultra-low values of $\kappa(T)$. Herein, it should be also noted that the applied model does not distinguish between three- and four-phonon decay mechanisms in umklapp processes, and as is known, the latter can lead to extremely low $\kappa(T)$, as it is the case for $PbCuSbS_3$.[73] Obviously, to shed more light on this problem, inelastic neutron scattering on single-crystalline $Yb_5Rh_6Sn_{18}$ combined with theoretical lattice dynamics studies would be required.

The possible occurrence of phonon resonance in $Yb_5Rh_6Sn_{18}$ could be the main reason for its ultra-low thermal conductivity. This phenomenon is usually described by a simple mechanical oscillator model given by eqn (12), where the half-width of the energy resonance curve is defined as $\Gamma = \omega_{PR}C_6/2$ and a proportionality factor containing the concentration of oscillators is $A = C_5/\Gamma$.[92] Since a resonance interaction with a relaxation time τ_{PR}^{-1} is believed to occur between phonons and defects, the enhanced C_2 parameter would nicely agree with this expectation. One of the central questions for such systems is the nature of the resonator. In early studies of mixed halides, this role was ascribed to the impurity non-magnetic ions,[92–94] whereas in the cage compounds to 'rattling' atoms.[96] However, the concept of inelastic resonance associated with energy dissipation of isolated 'rattling' atoms has

Table 5 Relaxation time constants (C_n) and the characteristic PR frequency (ω_{PR}) deduced from the fit to the modified Debye–Callaway model

τ^{-1}	Equation[97]	C_n
τ_B^{-1}	v_S/C_1	$4.0(1) \times 10^{-7}$ m
τ_{PD}^{-1}	$C_2x^4T^4$	$4.0(1) \times 10^5$ s^{-1} K^{-4}
τ_N^{-1}	$C_3x^3T^4$	$1.5(1) \times 10^3$ s^{-1} K^{-4}
τ_U^{-1}	$C_4x^2T^2e^{(-\Theta_D/3T)}$	$8.7(1) \times 10^5$ s^{-1} K^{-2}
τ_{PR}^{-1}	C_5	$5.1(1) \times 10^{35}$ s^{-3}
	C_6	2.1(1)
	ω_{PR}	5.8(1) THz

been recently challenged[99–101] by inelastic neutron scattering and lattice dynamics studies for clathrate- and skutterudite-based cage compounds. Since the value of the characteristic PR frequency ω_{PR}, deduced for $Yb_5Rh_6Sn_{18}$ from our fit, is comparable with that reported for the $Sr_8Ga_{16}Ge_{30}$ clathrate,[96] one could conclude on the same nature of the resonator (*i.e.*, 'rattling' atoms) in both substances. Despite being less understood and its applicability to thermal properties of cage compounds is debated,[72,102–104] PR would clearly contribute to a drastic reduction in $\kappa(T)$. For instance, as it has been shown in ref. 95, its appearance in PbS leads to a decrease of $\kappa_{ph}(T)$ by ≈70% at a certain temperature. Thus, since the lattice contribution is a dominant one in the case of $Yb_5Rh_6Sn_{18}$, its suppression plays a central role in the minimization of $\kappa_{tot}(T)$.

Due to their ultra-low thermal conductivity, clathrates and filled skutterudites are known to be promising thermoelectric (TE) materials, which is reflected in their enhanced dimensionless figure of merit $zT = S^2T/\rho\kappa > 1$.[87,90] In the case of $Yb_5Rh_6Sn_{18}$, the highest $zT = 5 \times 10^{-3}$ is observed at 40 K. The poor TE performance of this stannide is explained by the negligibly small Seebeck coefficient due to its predominantly metallic behavior.[79]

3.7 Electronic band structure

The atomic- and orbital-resolved electronic densities of states (DOS) of $Yb_5Rh_6Sn_{18}$ are presented in Fig. 9a and b, respectively. They show similar features to those reported earlier for the $Yb_3Rh_4Sn_{13}$ Remeika prototype[47] and the idealized structural model of $Sc_5Rh_6Sn_{18}$.[35] These are: (i) a low-lying energy band in the ≈−10.8 – ≈−5.8 eV range formed mainly by Sn-5s states, followed by (ii) an energy gap of ≈1 eV and (iii) a broad valence band extending from ∼−4.5 eV to the Fermi level E_F dominated mainly by Rh-4d and Sn-5p electrons.

As one can see from the inset in Fig. 9a and b, the majority of the states at E_F originate from Yb2-4f (≈41%), Sn-5p (≈29%), Yb1-4f (≈8%) and Rh-4d (≈9%) (the small admixture of Yb1,2-5d, Rh-5p, and Sn-5s together contributing ≈9% is not shown in the figures). Thus, in total, we obtain at the Fermi level a DOS of $D(E_F)$ = 18.8 states eV^{-1} f.u.$^{-1}$, which can be recalculated in a Sommerfeld coefficient of the electronic specific heat γ_{theor} = 44.5 mJ mol^{-1} K^{-2}. This value would be in acceptable agreement with those approximately estimated from the experiment. Taking into account that four electronic bands, with a curvature revealing no similarities to a parabola (Fig. S6†), cross E_F, one cannot expect that the simple free electron gas model would satisfactorily work in the case of $Yb_5Rh_6Sn_{18}$. Indeed, as it has been shown above, the electrical conduction mechanisms are found here to be of a complex nature.

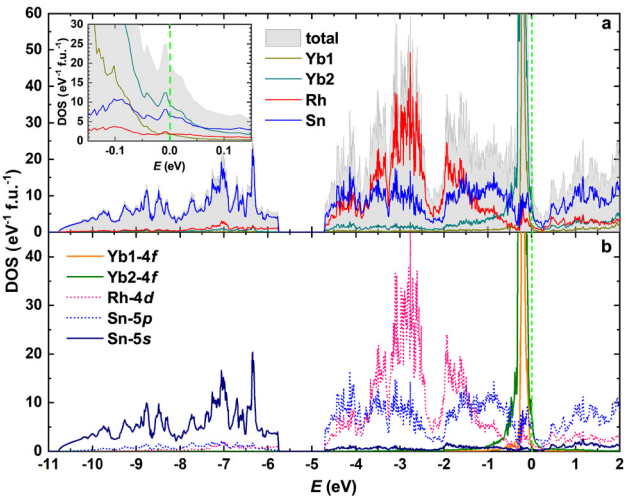

Fig. 9 (a) Total and atomic resolved electronic density of states (DOS) for $Yb_5Rh_6Sn_{18}$. Inset: DOS near the Fermi level E_F. (b) Orbital resolved DOSs. E_F is marked as a green dashed line.

4 Conclusions

$Yb_5Rh_6Sn_{18}$ crystallizes with a unique primitive tetragonal structural arrangement, which is closely related with the $Yb_3Rh_4Sn_{13}$ Remeika and $(Sn_{1-x}Tb_x)Tb_4Rh_6Sn_{18}$ types. Such a relationship is reflected in the unit cell parameters which are derived from $a \approx 9.5$ Å as well as in the common $[RhSn_6]$ corner sharing trigonal prismatic arrays with cuboctahedra incorporated into the free space in between. An important feature of the $Yb_5Rh_6Sn_{18}$ crystal structure is that the relatively small Sn1 atoms reside inside enlarged 16-vertices distorted Frank–Kasper polyhedra thus possessing potential for a 'rattling' motion. This expectation is confirmed by the fitting of the temperature dependence of specific heat capacity to the combined Debye–Einstein model. The Einstein temperature deduced from the fit is in good agreement with the value obtained from the thermal displacement parameter of the Sn1 atom refined from the powder XRD data.

The two white lines with temperature-dependent intensities in the X-ray absorption spectra (XAS) of $Yb_5Rh_6Sn_{18}$ indicate that the Yb ions are in the intermediate valence state (IVS) switching between the $4f^{13}$ (Yb^{3+}) and $4f^{14}$ (Yb^{2+}) configurations. The latter one was simulated by quantum mechanical density functional theory (DFT) calculations, which showed that the Yb2-5d states are unexpectedly strong, contributing to the Yb^{3+} white line. This finding can explain why the known theories fail to describe the IVS in the new stannide.

Indeed, the well-established Coqblin–Schrieffer model fails, whereas the Bickers–Cox–Wilkins one fairly describes the maximum in the temperature dependence of the magnetic susceptibility of $Yb_5Rh_6Sn_{18}$ only on the assumption of the J = 3/2 multiplet (degeneracy N = 4) which, however, is atypical for Yb atoms. Furthermore, the Kondo temperature of 191 K, obtained from such a fit, is much too low, which is not confirmed in further electrical transport studies.

Electrical resistivity, which increases with increasing temperature and fits well to the quadratic Fermi-liquid approach in the low-T regime, together with the observed small Seebeck coefficients as well as high charge carrier concentrations and their mobilities hints towards the metallic properties of

$Yb_5Rh_6Sn_{18}$. However, application of the free electron gas model failed in the description of electrical transport of this stannide. This fact is further ascribed to its complex electronic structure revealing four bands at the Fermi level (E_F) as well as to the temperature-dependent domination of the type of charge carrier (*i.e.*, electrons below ≈200 K and holes above).

A well-pronounced minimum in the *T*-dependent Seebeck coefficient is a feature indicating IVS. By applying a two-band theory, we found that the mean Yb valence is $\nu \approx 2.8$, if one assumes smaller degeneracy ($N = 4$), and it increases up to ≈2.9 for $N = 8$. Although both ν-values differ strongly from $\nu = 2.59$ to 2.62 (deduced from XAS), the observed tendency is in line with those found for magnetic susceptibility (*i.e.*, better description with models for smaller *N*).

$Yb_5Rh_6Sn_{18}$ shows an ultra-low thermal conductivity dominated by phonons in the low-*T* range. The lattice contribution shows also a clear minimum, which (at the level of this investigation) most likely can be attributed to the appearance of phonon resonance due to the 'rattling' motion of Sn1 atoms in the structure of this new stannide. Indeed, by applying the Debye–Callaway model, we deduced the characteristic resonance frequency [5.81 THz], which is comparable with the values for such cage compounds as intermetallic clathrates. Therefore, it is argued that the phonon resonance can explain why the thermal conductivity of $Yb_5Rh_6Sn_{18}$ becomes ultra-low.

Data availability

The data supporting this article are included as part of the ESI.†

Conflicts of interest

There are no conflicts of interest to declare.

Acknowledgements

The DynaCool-12 system was acquired within the DFG project 422219907. VL is grateful to DFG for financial support within the project 467257848. The authors thank H. Borrmann for performing the powder XRD analysis. We are also grateful to U. Burkhardt, S. Kostmann and P. Scheppan for the microstructural and EDX studies.

References

1 S. Engel, E. C. J. Gießelmann, M. K. Reimann, R. Pöttgen and O. Janka, *ACS Org. Inorg. Au*, 2024, **4**, 188–222.
2 P. S. Riseborough, *Adv. Phys.*, 2000, **49**, 257–320.
3 G. R. Stewart, *Rev. Mod. Phys.*, 2001, **73**, 797–855.
4 A. Georges, G. Kotliar, W. Krauth and M. J. Rozenberg, *Rev. Mod. Phys.*, 1996, **68**, 13–125.
5 C. M. Varma, *Rev. Mod. Phys.*, 1976, **48**, 219–238.
6 J. M. Lawrence, P. S. Riseborough and R. D. Parks, *Rep. Prog. Phys.*, 1981, **44**, 1–84.
7 P. W. Anderson, *Phys. Rev.*, 1961, **124**, 41–53.
8 J. Kondo, *Prog. Theor. Phys.*, 1964, **32**, 37–49.
9 N. E. Bickers, D. L. Cox and J. W. Wilkins, *Phys. Rev. B: Condens. Matter Mater. Phys.*, 1987, **36**, 2036–2079.
10 H. Bethe, *Z. Phys.*, 1931, **71**, 205–226.
11 B. Coqblin and J. R. Schrieffer, *Phys. Rev.*, 1969, **185**, 847–853.
12 A. M. Tsvelick and P. B. Wiegmann, *J. Phys. C: Solid State Phys.*, 1982, **15**, 1707.
13 V. T. Rajan, *Phys. Rev. Lett.*, 1983, **51**, 308–311.
14 A. Hewson, J. Rasul and D. Newns, *Solid State Commun.*, 1983, **47**, 59–61.
15 H.-U. Desgranges, *Phys. B*, 2015, **473**, 93–100.
16 A. Hewson, D. Newns, J. Rasul and N. Read, *J. Magn. Magn. Mater.*, 1985, **47–48**, 354–356.
17 E. Cattaneo, *Z. Phys. B: Condens. Matter*, 1986, **64**, 317–325.
18 H. Yamaoka, N. Tsujii, Y. Utsumi, H. Sato, I. Jarrige, Y. Yamamoto, J.-F. Lin, N. Hiraoka, H. Ishii, K.-D. Tsuei and J. Mizuki, *Phys. Rev. B: Condens. Matter Mater. Phys.*, 2013, **87**, 205120.
19 M. Kasaya, F. Iga, M. Takigawa and T. Kasuya, *J. Magn. Magn. Mater.*, 1985, **47–48**, 429–435.
20 H. Yamaoka, I. Jarrige, N. Tsujii, J.-F. Lin, N. Hiraoka, H. Ishii and K.-D. Tsuei, *Phys. Rev. B: Condens. Matter Mater. Phys.*, 2010, **82**, 035111.
21 J. Remeika, G. Espinosa, A. Cooper, H. Barz, J. Rowell, D. McWhan, J. Vandenberg, D. Moncton, Z. Fisk, L. Woolf, H. Hamaker, M. Maple, G. Shirane and W. Thomlinson, *Solid State Commun.*, 1980, **34**, 923–926.
22 R. Gumeniuk, L. Akselrud, K. O. Kvashnina, W. Schnelle, A. A. Tsirlin, C. Curfs, H. Rosner, M. Schöneich, U. Burkhardt, U. Schwarz, Y. Grin and A. Leithe-Jasper, *Dalton Trans.*, 2012, **41**, 6299–6309.
23 R. Gumeniuk, M. Schöneich, K. O. Kvashnina, L. Akselrud, A. A. Tsirlin, M. Nicklas, W. Schnelle, O. Janson, Q. Zheng, C. Curfs, U. Burkhardt, U. Schwarz and A. Leithe-Jasper, *Dalton Trans.*, 2015, **44**, 5638–5651.
24 R. Gumeniuk, M. Nicklas, L. Akselrud, W. Schnelle, U. Schwarz, A. A. Tsirlin, A. Leithe-Jasper and Y. Grin, *Phys. Rev. B: Condens. Matter Mater. Phys.*, 2013, **87**, 224502.
25 I. W. H. Oswald, B. K. Rai, G. T. McCandless, E. Morosan and J. Y. Chan, *CrystEngComm*, 2017, **19**, 3381–3391.
26 M. Feig, W. Carrillo-Cabrera, M. Bobnar, P. Simon, C. Curfs, V. Levytskyi, A. A. Tsirlin, A. Leithe-Jasper and R. Gumeniuk, *Dalton Trans.*, 2022, **51**, 4734–4748.
27 R. Gumeniuk, in *Handbook on the Physics and Chemistry of Rare Earths*, ed. J.-C. G. Bünzli and V. K. Pecharsky, Elsevier, 2018, vol. 54, pp. 43–143.
28 S. Miraglia, J. L. Hodeau, F. de Bergevin, M. Marezio and G. P. Espinosa, *Acta Crystallogr., Sect. B: Struct. Sci.*, 1987, **43**, 76–83.

29 S. C. Peter, U. Subbarao, S. Rayaprol, J. B. Martin, M. Balasubramanian, C. D. Malliakas and M. G. Kanatzidis, *Inorg. Chem.*, 2014, **53**, 6615–6623.
30 V. Levytskyi, W. Carrillo-Cabrera, L. Akselrud, B. Kundys, A. Leithe-Jasper and R. Gumeniuk, *Dalton Trans.*, 2022, **51**, 10036–10046.
31 A. Bhattacharyya, D. T. Adroja, N. Kase, A. D. Hillier, A. M. Strydom and J. Akimitsu, *Phys. Rev. B*, 2018, **98**, 024511.
32 N. Kase, K. Inoue, H. Hayamizu and J. Akimitsu, *J. Phys. Soc. Jpn.*, 2011, **80**, SA112.
33 A. Bhattacharyya, D. Adroja, N. Kase, A. Hillier, J. Akimitsu and A. Strydom, *Sci. Rep.*, 2015, **5**, 12926.
34 M. Feig, W. Schnelle, A. Maisuradze, A. Amon, C. Baines, M. Nicklas, S. Seiro, L. Howald, R. Khasanov, A. Leithe-Jasper and R. Gumeniuk, *Phys. Rev. B*, 2020, **102**, 024508.
35 M. Feig, L. Akselrud, W. Schnelle, V. Dyadkin, D. Chernyshov, A. Ormeci, P. Simon, A. Leithe-Jasper and R. Gumeniuk, *Dalton Trans.*, 2020, **49**, 6832–6841.
36 D. Kumar, C. N. Kuo, F. Astuti, T. Shang, M. K. Lee, C. S. Lue, I. Watanabe, J. A. T. Barker, T. Shiroka and L. J. Chang, *J. Phys.: Condens. Matter*, 2018, **30**, 315803.
37 V. Levytskyi, M. Feig, L. Akselrud, W. Schnelle, A. Leithe-Jasper, V. Dyadkin, D. Chernyshov and R. Gumeniuk, *J. Phys.: Condens. Matter*, 2019, **31**, 445603.
38 E. G. Moshopoulou, M. F. Hundley, R. Movshovich, J. D. Thompson, J. L. Sarrao, Z. Fisk, E. Felder, M. Chernikov, D. Pushin and H. R. Ott, *Phys. Rev. B: Condens. Matter Mater. Phys.*, 1999, **60**, 4096–4100.
39 A. D. Montero, G. T. McCandless, O. Oladehin, R. E. Baumbach and J. Y. Chan, *Chem. Mater.*, 2023, **35**, 2238–2247.
40 G. Espinosa, *Mater. Res. Bull.*, 1980, **15**, 791–798.
41 G. Espinosa, A. Cooper and H. Barz, *Mater. Res. Bull.*, 1982, **17**, 963–969.
42 J. Hodeau, M. Marezio, J. Remeika and C. Chen, *Solid State Commun.*, 1982, **42**, 97–102.
43 S. Miraglia, J. Hodeau, M. Marezio, C. Laviron, M. Ghedira and G. Espinosa, *J. Solid State Chem.*, 1986, **63**, 358–368.
44 P. Bordet, J. Hodeau, P. Wolfers, G. Krill, F. Weiss and M. Marezio, *J. Magn. Magn. Mater.*, 1987, **63–64**, 524–526.
45 B. K. Rai, I. W. H. Oswald, J. Y. Chan and E. Morosan, *Phys. Rev. B*, 2016, **93**, 035101.
46 M. Feig, L. Akselrud, M. Motylenko, M. Bobnar, J. Wagler, K. O. Kvashnina, V. Levytskyi, D. Rafaja, A. Leithe-Jasper and R. Gumeniuk, *Dalton Trans.*, 2021, **50**, 13580–13590.
47 R. Gumeniuk, V. Levytskyi, B. Kundys and A. Leithe-Jasper, *Phys. Rev. B*, 2023, **108**, 214515.
48 *STOE Powder Software, WinXPow (version 2)*, Darmstadt, STOE and Cie GmbH, 2001.
49 L. Akselrud and Y. Grin, *J. Appl. Crystallogr.*, 2014, **47**, 803–805.
50 G. M. Sheldrick, *Acta Crystallogr., Sect. A: Found. Crystallogr.*, 2008, **64**, 112–122.
51 L. J. Farrugia, *J. Appl. Crystallogr.*, 2012, **45**, 849–854.
52 A. C. Scheinost, J. Claussner, J. Exner, M. Feig, S. Findeisen, C. Hennig, K. O. Kvashnina, D. Naudet, D. Prieur, A. Rossberg, M. Schmidt, C. Qiu, P. Colomp, C. Cohen, E. Dettona, V. Dyadkin and T. Stumpf, *J. Synchrotron Radiat.*, 2021, **28**, 333–349.
53 K. O. Kvashnina and A. C. Scheinost, *J. Synchrotron Radiat.*, 2016, **23**, 836–841.
54 V. Solé, E. Papillon, M. Cotte, P. Walter and J. Susini, *Spectrochim. Acta, Part B*, 2007, **62**, 63–68.
55 K. Koepernik and H. Eschrig, *Phys. Rev. B: Condens. Matter Mater. Phys.*, 1999, **59**, 1743–1757.
56 J. P. Perdew and Y. Wang, *Phys. Rev. B: Condens. Matter Mater. Phys.*, 1992, **45**, 13244.
57 J. Emsley, *The Elements*, Clarendon Press, Oxford, 1998.
58 J. Vandenberg, *Mater. Res. Bull.*, 1980, **15**, 835–847.
59 R. Gumeniuk, R. Sarkar, C. Geibel, W. Schnelle, C. Paulmann, M. Baenitz, A. A. Tsirlin, V. Guritanu, J. Sichelschmidt, Y. Grin and A. Leithe-Jasper, *Phys. Rev. B: Condens. Matter Mater. Phys.*, 2012, **86**, 235138.
60 R. Sarkar, R. Gumeniuk, A. Leithe-Jasper, W. Schnelle, Y. Grin, C. Geibel and M. Baenitz, *Phys. Rev. B: Condens. Matter Mater. Phys.*, 2013, **88**, 201101.
61 A. Ochiai, T. Suzuki and T. Kasuya, *J. Phys. Soc. Jpn.*, 1990, **59**, 4129–4141.
62 V. H. Tran, W. Miiller, A. Kowalczyk, T. Tolinski and G. Chelkowska, *J. Phys.: Condens. Matter*, 2006, **18**, 10353.
63 A. Kowalczyk, M. Falkowski and T. Tolinski, *J. Appl. Phys.*, 2010, **107**, 123917.
64 A. Grytsiv, D. Kaczorowski, A. Leithe-Jasper, P. Rogl, M. Potel, H. Noël, A. Pikul and T. Velikanova, *J. Solid State Chem.*, 2002, **165**, 178–181.
65 J. W. Rasul and A. C. Hewson, *J. Phys. C: Solid State Phys.*, 1984, **17**, 2555–2573.
66 B. C. Sales and D. K. Wohlleben, *Phys. Rev. Lett.*, 1975, **35**, 1240–1244.
67 L. B. Farhat, M. Amami, E. Hlil and R. B. Hassen, *J. Alloys Compd.*, 2009, **485**, 701–705.
68 A. Bhattacharyya, D. T. Adroja, J. Quintanilla, A. D. Hillier, N. Kase, A. M. Strydom and J. Akimitsu, *Phys. Rev. B: Condens. Matter Mater. Phys.*, 2015, **91**, 060503.
69 J. Wu, J. Xu and K. Tanigaki, *J. Phys. Chem. Solids*, 2024, **184**, 111709.
70 Y. Ikeuchi, H. Takatsu, C. Tassel, C. M. Brown, T. Murakami, Y. Matsumoto, Y. Okamoto and H. Kageyama, *Inorg. Chem.*, 2019, **58**, 6790–6795.
71 M. Beekman, W. Schnelle, H. Borrmann, M. Baitinger, Y. Grin and G. S. Nolas, *Phys. Rev. Lett.*, 2010, **104**, 018301.
72 S. Pailhes, V. Giordano, S. Turner, P.-F. Lory, C. Candolfi, M. de Boissieu and H. Euchner, *Results Phys.*, 2023, **49**, 106487.
73 E. Zuñiga-Puelles, R. Cardoso-Gil, A. Özden, N. Bulut, V. Svitlyk, C. Himcinschi, J. Kortus and R. Gumeniuk, *Phys. Rev. B*, 2022, **106**, 195201.
74 E. Zuñiga-Puelles, A. Özden, V. Pacheco, L. Akselrud, R. Cardoso-Gil, A. Straßheim, P. Wyżga, C. Himcinschi and R. Gumeniuk, *J. Alloys Compd.*, 2024, **976**, 173055.

75 W. Schnelle, A. Leithe-Jasper, H. Rosner, R. Cardoso-Gil, R. Gumeniuk, D. Trots, J. A. Mydosh and Y. Grin, *Phys. Rev. B: Condens. Matter Mater. Phys.*, 2008, **77**, 094421.
76 M. M. Koza, A. Leithe-Jasper, H. Rosner, W. Schnelle, H. Mutka, M. R. Johnson, M. Krisch, L. Capogna and Y. Grin, *Phys. Rev. B: Condens. Matter Mater. Phys.*, 2011, **84**, 014306.
77 A. Wang, Z. Y. Nie, F. Du, G. M. Pang, N. Kase, J. Akimitsu, Y. Chen, M. J. Gutmann, D. T. Adroja, R. S. Perry, C. Cao, M. Smidman and H. Q. Yuan, *Phys. Rev. B*, 2021, **103**, 024503.
78 Z. Zhang, Y. Xu, C. N. Kuo, X. C. Hong, M. X. Wang, P. L. Cai, J. K. Dong, C. S. Lue and S. Y. Li, *Supercond. Sci. Technol.*, 2015, **28**, 105008.
79 R. Groos and A. Marx, *Festkörperphysik*, Oldenbourg Verlag München, 2012.
80 N. Mott and H. Jones, *The Theory of the Properties of Metals and Alloys*, Dover Publications, New York, 1958.
81 R. Gumeniuk, K. Kvashnina, W. Schnelle, M. Nicklas, H. Borrmann, H. Rosner, Y. Skourski, A. A. Tsirlin, A. Leithe-Jasper and Y. Grin, *J. Phys.: Condens. Matter*, 2011, **23**, 465601.
82 K. Kadowaki and S. Woods, *Solid State Commun.*, 1986, **58**, 507–509.
83 Y. Bando, T. Suemitsu, K. Takagi, H. Tokushima, Y. Echizen, K. Katoh, K. Umeo, Y. Maeda and T. Takabatake, *J. Alloys Compd.*, 2000, **313**, 1–6.
84 U. Gottwick, K. Gloss, S. Horn, F. Steglich and N. Grewe, *J. Magn. Magn. Mater.*, 1985, **47–48**, 536–538.
85 P. M. Chaikin and G. Beni, *Phys. Rev. B: Solid State*, 1976, **13**, 647–651.
86 J. F. Kwak and G. Beni, *Phys. Rev. B: Solid State*, 1976, **13**, 652–657.
87 M. Baitinger, B. Böhme, A. Ormeci and Y. Grin, in *Solid State Chemistry of Clathrate Phases: Crystal Structure, Chemical Bonding and Preparation Routes*, ed. G. S. Nolas, Springer, Netherlands, Dordrecht, 2014, pp. 35–64.
88 D. O. Lindroth, J. Brorsson, E. Fransson, F. Eriksson, A. Palmqvist and P. Erhart, *Phys. Rev. B*, 2019, **100**, 045206.
89 J. Shen, T. Xie, L. Zhang, P. Wang and Z. Fang, *Sci. Rep.*, 2020, **10**, 3068.
90 *Recent Trends in Thermoelectric Materials Research I*, ed. T. M. Tritt, Elsevier, 2001, vol. 69 of Semiconductors and Semimetals, pp. 139–253.
91 H.-S. Kim, Z. M. Gibbs, Y. Tang, H. Wang and G. J. Snyder, *APL Mater.*, 2015, **3**, 041506.
92 R. O. Pohl, *Phys. Rev. Lett.*, 1962, **8**, 481–483.
93 F. C. Baumann, J. P. Harrison, R. O. Pohl and W. D. Seward, *Phys. Rev.*, 1967, **159**, 691–699.
94 R. F. Caldwell and M. V. Klein, *Phys. Rev.*, 1967, **158**, 851–875.
95 E. Zuñiga-Puelles, V. Levytskyi, A. Özden, T. Gürel, N. Bulut, C. Himcinschi, C. Sevik, J. Kortus and R. Gumeniuk, *Phys. Rev. B*, 2023, **107**, 195203.
96 J. L. Cohn, G. S. Nolas, V. Fessatidis, T. H. Metcalf and G. A. Slack, *Phys. Rev. Lett.*, 1999, **82**, 779–782.
97 T. M. Tritt, *Thermal conductivity: theory, properties, and applications*, Springer Science & Business Media, 2005.
98 K. Gofryk, D. Kaczorowski, T. Plackowski, J. Mucha, A. Leithe-Jasper, W. Schnelle and Y. Grin, *Phys. Rev. B: Condens. Matter Mater. Phys.*, 2007, **75**, 224426.
99 M. M. Koza, M. R. Johnson, R. Viennois, H. Mutka, L. Girard and D. Ravot, *Nat. Mater.*, 2008, **7**, 805–810.
100 M. Christensen, A. B. Abrahamsen, N. B. Christensen, F. Juranyi, N. H. Andersen, K. Lefmann, J. Andreasson, C. R. H. Bahl and B. B. Iversen, *Nat. Mater.*, 2008, **7**, 811–815.
101 A. Bhattacharya, *J. Mater. Chem. C*, 2019, **7**, 13986–13992.
102 E. S. Toberer, A. Zevalkink and G. J. Snyder, *J. Mater. Chem.*, 2011, **21**, 15843–15852.
103 W. Li and N. Mingo, *Phys. Rev. B: Condens. Matter Mater. Phys.*, 2015, **91**, 144304.
104 M. Baggioli, B. Cui and A. Zaccone, *Phys. Rev. B*, 2019, **100**, 220201.